Nematic confined phases in the U(1) quantum link model on a triangular lattice: Near-term quantum computations of string dynamics on a chip

D. Banerjee [1] S. Caspar [2] F.-J. Jiang [3] J.-H. Peng [3] and U.-J. Wiese [4]

[1]*Saha Institute of Nuclear Physics, HBNI, 1/AF Bidhannagar, Kolkata 700064, India*
[2]*InQubator for Quantum Simulation, Department of Physics, University of Washington, Seattle, Washington 98195, USA*
[3]*Department of Physics, National Taiwan Normal University 88, Ting-Chou Road, Taipei 116, Taiwan*
[4]*Albert Einstein Center, Institute for Theoretical Physics, University of Bern, 3012 Bern, Switzerland*

The U(1) quantum link model on the triangular lattice has two rotation-symmetry-breaking nematic confined phases. Static external charges are connected by confining strings consisting of individual strands with fractionalized electric flux. The two phases are separated by a weak first-order phase transition with an emergent, almost exact SO(2) symmetry. We construct a quantum circuit on a chip to facilitate near-term quantum computations of the nontrivial string dynamics.

I. INTRODUCTION

The confinement of quarks and gluons inside hadrons is a central dynamical mechanism in quantum chromodynamics (QCD). In a pure Yang-Mills theory, in which quarks appear only as static external color charges, quarks and antiquarks are connected by unbreakable confining strings. At large distances r the static quark-antiquark potential $V(r) \sim \sigma r$ is dominated by the string tension σ. The strings themselves are interesting dynamical objects that support massless excitations, which are described by a systematic low-energy effective theory of Goldstone bosons [1–3]. This low-energy effective string theory predicts the universal subleading Lüscher term correction to $V(r)$. In the presence of a static quark-antiquark pair some spatial symmetries as well as charge conjugation are explicitly broken. The string excitations can be classified by the irreducible representations of the remaining unbroken subgroup and are again predicted by the effective string theory. The dynamics of the string have been studied in great detail by Monte Carlo simulations in the framework of Wilson's lattice gauge theory [4–11] and quantitative agreement with the low-energy effective theory has been established.

Quantum link models [12–16] provide a generalization of Wilson's framework of lattice gauge theory [17]. In contrast to the Wilson theory, quantum link models have a finite-dimensional link Hilbert space while still maintaining exact gauge symmetry. Quantum link models capture a wider range of physical phenomena than those that are accessible in the Wilson framework. This includes crystalline confined phases [18], which are characterized by the spontaneous breakdown of lattice translation symmetry as well as the splitting of confining strings into individual strands that carry fractionalized electric flux, both in Abelian [19] and in non-Abelian [20] quantum link models. The $(2 + 1)$-dimensional U(1) quantum link model was investigated in [19,21–35]. Quantum dimer models [36] in condensed matter physics have the same Hamiltonian as the U(1) quantum link model on the square lattice, but realize the Gauss law in an unconventional manner. They also display crystalline confinement and flux fractionalization [37,38].

Quantum link models are not limited to these phenomena, but can even be used as a regularization of QCD itself [15]. Gluon fields then emerge as collective excitations of discrete quantum link variables and quarks arise as domain wall fermions. Due to the finite-dimensional link Hilbert space of quantum link models, this alternative formulation of QCD is well suited for the implementation in quantum simulation experiments [39–41]. In particular, quarks and gluons can be embodied by ultracold alkaline-earth atoms in an optical superlattice [42]. Quantum simulator constructions for U(1) quantum link models with dynamical fermions have used ultracold Bose-Fermi mixtures in optical superlattices [43], while constructions without fermions have been based on Rydberg atoms in optical lattices [44] or on superconducting quantum circuits [45]. Experimental digital as well as analog quantum simulations or computations of lattice gauge theories including quantum link models have been realized in [46–54]. The anticipated realization of quantum link models in further forthcoming quantum computations and quantum simulation experiments motivates the detailed investigation of their intricate confinement phases.

Near-term devices such as IBM's 127-qubit Eagle chip [55,56] offer unique opportunities for the quantum computation of simple gauge theories that share important properties with QCD, without the need to perform highly nontrivial experiments. Here we consider a U(1) quantum link model

---

on a triangular lattice, which is equivalent to a dual height model on a hexagonal lattice that ideally matches the heavy hexagonal topology of the Eagle chip [57]. The height variables are directly embodied by individual qubits. This allows us to study the intriguing real-time dynamics of confining strings, which in this case also represent interfaces separating distinct nematic confined phases. In those phases lattice rotation invariance is spontaneously broken while translation invariance remains intact (cf. [58–63]). Here we study the confining dynamics in $2 + 1$ dimensions, using near-term quantum hardware, without taking a continuum limit.

II. MODELS AND OBSERVABLES

We consider a U(1) quantum link model on a triangular lattice, with a two-dimensional link Hilbert space analogous to a quantum spin $\frac{1}{2}$. The two link states carry electric fluxes $\pm\frac{1}{2}$. The Hamiltonian takes the form

$$H = \sum_\triangle H_\triangle = -J \sum_\triangle [U_\triangle + U_\triangle^\dagger - \lambda(U_\triangle + U_\triangle^\dagger)^2]. \quad (1)$$

Here $U_\triangle = U_{xy}U_{yz}U_{zx}$ is an operator associated with the parallel transport around a triangular plaquette $\triangle$. It is built from quantum link operators U_{xy} connecting nearest-neighbor sites x and y. A U(1) quantum link $U_{xy} = S_{xy}^1 + iS_{xy}^2 = S_{xy}^+$ is a raising operator of electric flux $E_{xy} = S_{xy}^3$, constructed from a quantum spin $\frac{1}{2}$, S_{xy}^a ($a \in \{1, 2, 3\}$), associated with the link xy. The first term in the Hamiltonian inverts a closed loop of electric flux around a triangular plaquette. It also annihilates nonflippable plaquette states, i.e., those that do not contain a closed flux loop. The Rokhsar-Kivelson term, proportional to λ, counts flippable plaquettes. The Hamiltonian commutes with the generators of infinitesimal U(1) gauge transformations, which correspond to the lattice divergence of the electric flux operators,

$$G_x = \sum_{i=1,2,3} (E_{x,x+\hat{i}} - E_{x-\hat{i},x}). \quad (2)$$

Here $\hat{i}$ denotes unit vectors in three lattice directions separated by $120°$ angles. In the absence of external charges, physical states $|\Psi\rangle$ obey the Gauss law $G_x|\Psi\rangle = 0$. When static external charges $Q_x \in \{\pm 1, \pm 2, \pm 3\}$ are installed at the lattice sites x, the Gauss law is modified to $G_x|\Psi\rangle = Q_x|\Psi\rangle$. Besides the U(1) gauge symmetry, there are several global symmetries, including lattice translations, rotations, and reflections, and charge conjugation C, which replaces U_{xy} by $U_{xy}^\dagger$ and E_{xy} by $-E_{xy}$. We consider a rhombic lattice of side length L with periodic boundary conditions, which is equivalent to a regular hexagon with side length $L/\sqrt{3}$, thus maintaining all lattice symmetries even in a finite volume. The torus topology implies an additional global U(1)^2 center symmetry associated with large gauge transformations [64]. The corresponding superselection sectors are characterized by wrapping electric fluxes $F_1 = E_2 - E_3$, $F_2 = E_3 - E_1$, and $F_3 = E_1 - E_2$, where $E_i = \frac{1}{L}\sum_x E_{x,x+\hat{i}} \in \mathbb{Z}/2$. The $F_i \in \mathbb{Z}$ commute with the Hamiltonian, but cannot be expressed through small periodic gauge transformations G_x. It should be noted that the three F_i are not independent because $F_1 + F_2 + F_3 = 0$.

It is natural to introduce dual degrees of freedom: quantum height variables which are associated with the hexagonal lattice that is dual to the original triangular lattice. The dual hexagonal lattice is bipartite and consists of two sublattices A and B. The height variables on sublattice A are associated with the center $\tilde{x}$ of an original triangle and take values $h_{\tilde{x}}^A \in \{0, 1\}$, while the height variables on sublattice B take the half-integer values $h_{\tilde{x}}^B \in \{-\frac{1}{2}, \frac{1}{2}\}$. A configuration of height variables is associated with a flux configuration

$$E_{x,x+\hat{i}} = (h_{\tilde{x}}^A - h_{\tilde{x}'}^B)\text{mod}2 = \pm\frac{1}{2}. \quad (3)$$

Here $\tilde{x} = x + \frac{1}{3}(\hat{i} - \hat{j})$ and $\tilde{x}' = x + \frac{1}{3}(\hat{i} - \hat{k})$, where $j = (i - 1)\text{mod}3$ and $k = (i + 1)\text{mod}3$. It should be noted that, for a given flux configuration, the height variables are uniquely defined only up to a global shift $h_{\tilde{x}}^X \to [h_{\tilde{x}}^X + 1]\text{mod}2$ ($X \in \{A, B\}$). The introduction of the dual height variables guarantees that the Gauss law of the original flux variables is automatically satisfied modulo 2. In order to impose the full Gauss law, the height variables are subject to a corresponding constraint. In order to define the height variables in the presence of odd charges $Q_x \in \{\pm 1, \pm 3\}$, one must connect these charges by Dirac strings running along the links of the original triangular lattice. Across a Dirac string, one of the adjacent height variables must be shifted by 1 modulo 2.

In order to identify the symmetry-breaking patterns in the different phases, we introduce two order parameters

$$M_A = \frac{2}{L^2}\sum_{\tilde{x}\in A}\left(h_{\tilde{x}}^A - \frac{1}{2}\right), \quad M_B = \frac{2}{L^2}\sum_{\tilde{x}\in B}h_{\tilde{x}}^B, \quad (4)$$

associated with the two sublattices (each with L^2 plaquettes such that $M_A, M_B \in [-1, 1]$). Due to the global shift ambiguity of the height variables, (M_A, M_B) and $(-M_A, -M_B)$ are physically equivalent. It is important to understand the transformation behavior of the order parameters under the following symmetries: the charge conjugation C, the $60°$ rotation O around a point on the triangular lattice, the reflection R on a lattice axis, and the reflection $R' = RO$ on an axis orthogonal to a lattice axis. The order parameters transform as

$$\begin{aligned} {}^C M_A &= M_A, & {}^C M_B &= -M_B, \\ {}^O M_A &= M_B, & {}^O M_B &= -M_A, \\ {}^R M_A &= M_B, & {}^R M_B &= M_A, \\ {}^{R'} M_A &= M_A, & {}^{R'} M_B &= -M_B. \end{aligned} \quad (5)$$

III. METHOD AND NUMERICAL RESULTS

It is straightforward to set up a Euclidean time path integral for the canonical partition function $Z = \text{Tr}[\exp(-\beta H)P]$ (at inverse temperature β) using the dual height variable representation. Here the operator P, which commutes with the Hamiltonian, imposes the Gauss law by projecting onto the Hilbert space of physical states. We have developed an efficient quantum Monte Carlo cluster algorithm (cf. [20,65]) that operates on the height variables, one sublattice at a time. Equal-value height variables are connected to clusters according to rules that guarantee detailed balance. Special rules apply in the last time slice in which the projection operator P enforces the Gauss law. The algorithm has been implemented in continuous Euclidean time [66].
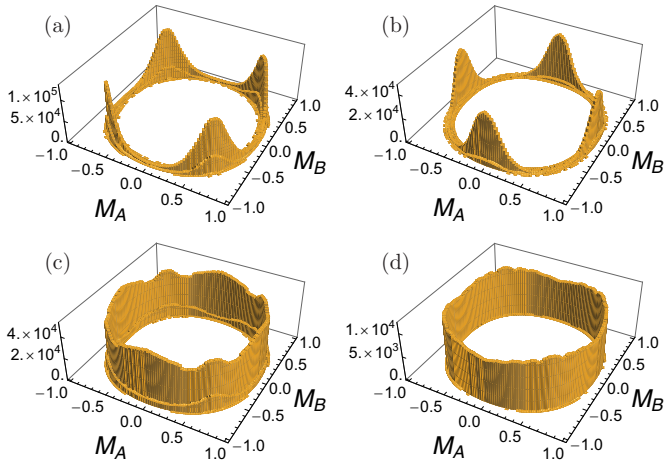
FIG. 1. Order parameter distributions in the (M_A, M_B) plane for $L = 64$ at (a) $\lambda = -0.2156$, (b) $\lambda = -0.2146$, and (c) $\lambda = -0.2152$ and for $L = 48$ at (d) $\lambda = -0.214\,425$.

FIG. 2. Energy distribution for the strings connecting two charges (a) ± 1 at distance $r = 15\sqrt{3}$ and (b) ± 2 at $r = 26$, with $\lambda = -0.1 > \lambda_c$, as well as (c) ± 3 at distance $r = 15\sqrt{3}$ and (d) ± 2 at $r = 26$, with $\lambda = -0.3 < \lambda_c$.

In order to explore the phase structure, first in the absence of external charges, we have performed Monte Carlo simulations on systems with $L = 8, 16, 32, 48, 64$ at temperatures corresponding to $\beta J = L$. We have explored the region $\lambda \leqslant 0$ where the cluster algorithm is applicable. Figure 1 shows the probability distribution of the order parameters (M_A, M_B) for different values of λ. For $\lambda > \lambda_c = -0.215(1)$ [Fig. 1(a)] the height variables on one of the two sublattices are ordered (either $M_A \neq 0$ or $M_B \neq 0$), which implies that the $60°$ rotation symmetry O is spontaneously broken. For $\lambda < \lambda_c$ [Fig. 1(b)], on the other hand, both sublattices are ordered. This implies that, in addition to O, also C is broken. Since translational invariance remains intact in both phases, we encounter two distinct nematic phases.

Remarkably, the phase transition at λ_c is associated with an emergent, almost exact spontaneously broken SO(2) symmetry, which manifests itself in the ring-shaped order parameter distribution shown in Fig. 1(c). The corresponding pseudo-Goldstone boson is dual to an almost massless photon. Thus, the model mimics certain aspects of a deconfined quantum critical point [67,68]. However, unlike for deconfined quantum criticality, the radius of the ring-shaped order parameter distribution does not shrink to zero at the transition. A similar behavior was first observed for the U(1) quantum link model on the square lattice [19], but has also been found in other systems [69]. As a result, the transition that separates the two distinct nematic phases is an exotic first-order phase transition, with an order parameter that remains large at the transition, while there is still a large correlation length due to the almost massless emergent pseudo-Goldstone boson. At present, we do not understand the origin of these long-range correlations. Weak first-order phase transitions have been associated with slowly walking couplings near a conformal point [70]. While it would be interesting to explore this idea in the context of the U(1) quantum link model, in this paper we focus on the corresponding confining string dynamics.

We now proceed to the physics in the presence of external charges. We begin with the phase at $\lambda > \lambda_c$ in which O but not C is spontaneously broken. Figure 2(a) illustrates the energy
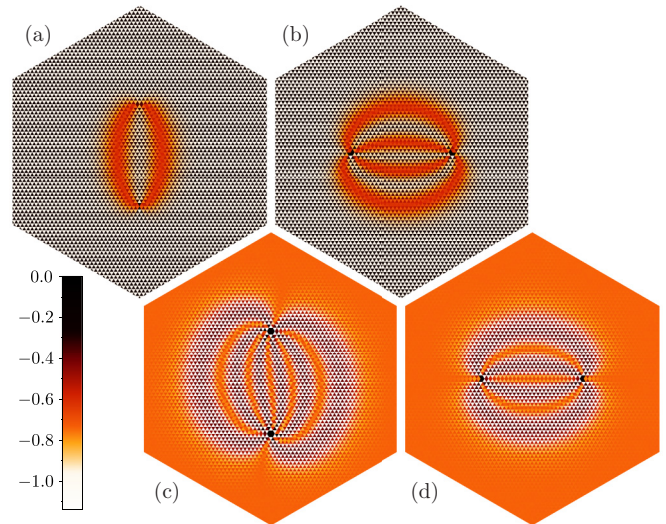
density of the confining string that connects two charges ± 1 separated along a line that is orthogonal to a lattice axis. The string separates into two distinct strands, each carrying a fractionalized flux $\frac{1}{2}$. The strands are interfaces that separate the two degenerate bulk phases. Indeed, in the region between the strands the flippable triangular plaquettes are on sublattice B, while they are on sublattice A in the surrounding bulk. The external charges are responsible for an explicit breaking of translation invariance, of the charge conjugation C, and of the rotation O. There are two types of reflections that are not explicitly broken in the presence of the external charges. One is the reflection R' on the line connecting the charges. The other is a combination of C with the reflection R on the lattice axis that maps the charges onto each other. While R' is not spontaneously broken in the bulk, the combination CR is. Not unexpectedly, the spontaneous breakdown of CR in the surrounding bulk manifests itself in a very slight asymmetry in the strands. Figure 2(b) shows the situation with two external charges ± 2 separated along a lattice axis. The string then fractionalizes into four strands which separate regions of alternating bulk phases. In this case, neither R nor CR' is explicitly broken by the external charges, but the spontaneous breakdown of R in the bulk is responsible for a visible asymmetry in the strand geometry.

Next we consider the other nematic phase with $\lambda < \lambda_c$ in which both O and C are spontaneously broken. Figure 2(c) shows the structure of a string connecting two charges ± 3 separated along a line orthogonal to a lattice axis. First of all, the string now fractionalizes into six strands, which again separate alternating bulk phases. Interestingly, the interior of the strands consists of the bulk phase that occurs on the other side of the phase transition. As before, for the present arrangement of charges the symmetries R' and CR are not explicitly broken. However, unlike in the nematic phase with $\lambda > \lambda_c$, for $\lambda < \lambda_c$ not only CR but also R' is spontaneously broken in the bulk, while the combination CRR' remains unbroken. This
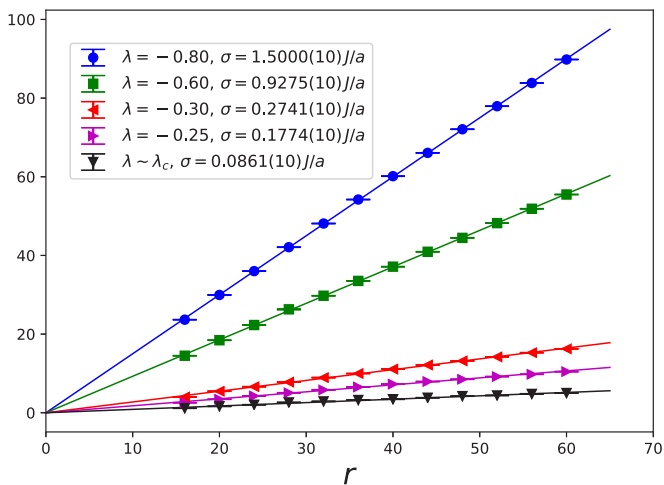
FIG. 3. Static charge-anticharge potential $V(r) \sim \sigma r$ as a function of the separation r and the corresponding string tension σ for various values of λ.

explains the symmetry of the corresponding strand geometry. Two charges ± 2 separated along a lattice axis are shown in Fig. 2(d). As before, in this situation both R and CR' are not explicitly broken. However, for $\lambda < \lambda_c$ neither R nor CR' is spontaneously broken, which explains the reflection symmetries in the corresponding strand geometry.

Let us consider the static charge-anticharge potential $V(r)$ in the nematic confinement phase with $\lambda < \lambda_c$ for two charges ± 2 separated along a lattice axis, as in Fig. 2(d). As expected, at large separation r the potential is linearly rising, i.e., $V(r) \sim \sigma r$ with the string tension σ (cf. Fig. 3). As one approaches λ_c, σ becomes very small but does not go to zero, indicating again that the phase transition is weakly first order. The minimal value of σ is reached at the transition.

Finally, we realize the model as a quantum circuit that embodies the effective string theory on a chip. The dual formulation can also be used to perform real-time simulations of the U(1) quantum link model. Since the Gauss law constraint is partially solved, this leads to a denser encoding of the physical Hilbert space than working directly with the flux degrees of freedom $E_{xy} = S_{xy}^3$ [25]. Each dual height variable $h^{A,B}$ maps exactly to one qubit $|a, b = 0, 1\rangle$ ($a = h^A$ and $b = h^B + \frac{1}{2}$). The electric field of Eq. (3) is diagonal in this basis and can be written in terms of the adjacent qubit operators $E_{x,x+\hat{i}} = Z_x^A Z_{x'}^B / 2$. While there are no self-adjoint single-link parallel transporters $U_{x,x+\hat{i}}$ in the dual formulation, operators for closed loops still exist. Plaquette operators $U_\triangle$ are generically four-qubit operators acting on the plaquette qubit A and its three nearest neighbors $B_{1,2,3}$ (see Fig. 4). The single-plaquette Hamiltonian $H_\triangle = -J(U_\triangle + U_\triangle^\dagger)$ can be written as a sum of seven mutually commuting Pauli strings with a weight of at most 3 (plus an irrelevant constant), due to cancellations of all terms of weight 4,

$$H_\triangle = \frac{J}{4}(1 + Z_1 Z_2 + Z_2 Z_3 + Z_3 Z_1)(\lambda - X_0). \quad (6)$$

This leads to a significant complexity reduction for quantum simulation compared to the same model on the square lattice. The square lattice Hamiltonian contains four- and five-qubits
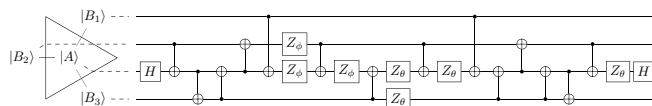

FIG. 4. Circuit decomposition of a single plaquette Trotter step $U = \exp(-iH_\triangle t)$. The two Hadamard gates H fully diagonalize the Hamiltonian. Each of the seven Pauli Z strings can be simulated independently by a single-qubit $Z_{\phi,\theta}$ rotation ($\theta = -Jt/2$ and $\phi = J\lambda t/2$), after reducing their Pauli weight with nearest-neighbor CNOT gates.

terms, which are more challenging to engineer on hardware with native few-body interactions. Additionally, the triangular lattice model in its dual formulation is ideally suited for studies on hardware with sparse connectivity, such as the heavy hexagonal lattice topology [57] underlying the recently unveiled 127-qubit IBM Eagle chip, as well as their lineup of future chips [56].

A possible circuit decomposition of a single plaquette unitary $U = \exp(-iH_\triangle t)$ with only nearest-neighbor CNOT gates, single-qubit Z rotations $Z_\theta = \exp(-i\theta Z/2)$, and Hadamard gates $H = (X + Z)/\sqrt{2}$ is shown in Fig. 4. Time evolution of the full system is achieved by separating the plaquettes of the A and B sublattices into alternating Trotter steps. Each plaquette unitary fully preserves the residual Gauss law.

A small-scale example of the dynamics that can already be studied on existing devices (e.g., on IBM's Falcon) is given in Fig. 5. Here the system is a parallelogram of eight plaquettes with fixed boundary conditions $a, b = 0$ on all external plaquettes. The system is initialized in the ground state of H_A, the sum of all plaquette terms on sublattice A (white triangles), which is just a product state. The quenched dynamics using the full Hamiltonian $H = H_A + H_B$ then leads to an oscillation between the order parameters (4) of sublattices A and B. This system also contains a flux string $E = \frac{1}{2}$ connecting fractional charges $\pm\frac{1}{2}$ at the top and bottom corners. Initially the flux
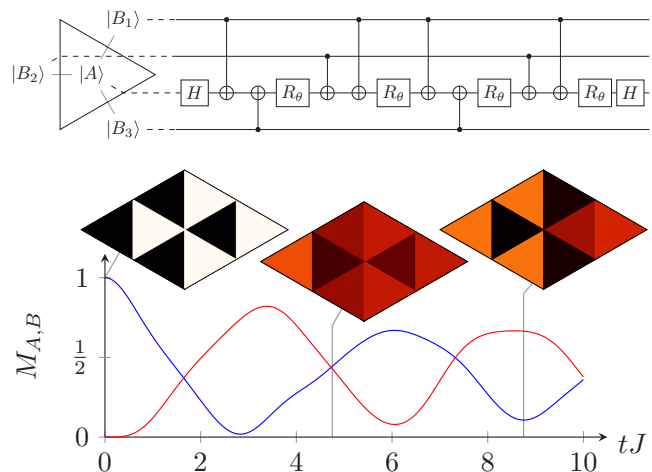

FIG. 5. (a) Circuit decomposition of $\exp(-iH_\triangle t)$ at $\lambda = 0$, using two Hadamard gates H, four single-qubit rotations R_θ with $\theta = -Jt/2$, and eight CNOT gates. (b) Real-time evolution of the order parameters $M_{A,B}$ on eight plaquettes. The energy density is illustrated at three times $tJ = 0, 4.75, 8.75$ in the same way as in Fig. 2.
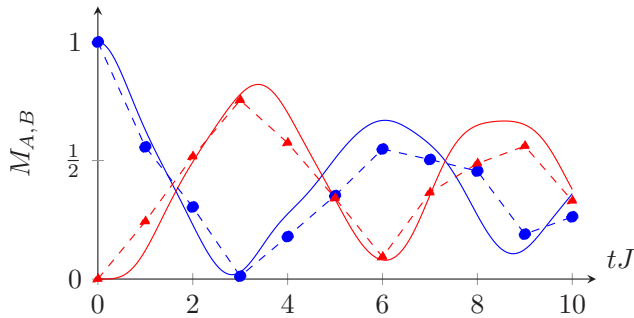
FIG. 6. Trotter evolution of magnetization order parameters M_A and M_B (y axis) versus real-time tJ (on the x axis) for the circuit proposed in Fig. 5 for $Jdt = 1.0$. The results in the time continuum are shown by solid lines, while the symbols connected by dashed lines indicate the first-order Trotter evolution. It is evident that the real-time oscillatory dynamics of the order parameters is qualitatively captured in this approximation.

runs along the left boundary, but then oscillates along with the order parameters, as shown in Fig. 5(b). It is curious to note that the fluctuations in the order parameter are coherent over reasonably long times, approximately ten times the natural timescale of the model, set by J. Such long-lived oscillations are typically indicative of slow thermalization and weak ergodicity breaking of the underlying model [71].

Since the quench is done with the Hamiltonian at $\lambda = 0$, the quantum circuit shown in Fig. 4 can be considerably simplified and can be expressed very compactly in Fig. 5(a). The use of eight CNOT gates makes this circuit highly attractive to implement in a quantum computer, like IBMQ Falcon. A valid concern is how much of the oscillatory dynamics of the order parameters is visible to the discretized Trotter evolution. In Fig. 6 we show the exact first-order Trotter evolution of the order parameters M_A and M_B for a step size $Jdt = 1.0$ and for a total of ten Trotter steps (symbols), superimposed on the data from Fig. 5(b) (shown by solid lines). It is immediately clear that even $dt = 1.0$ captures the relevant dynamics qualitatively. We estimate that about four Trotter steps are sufficient to capture this initial evolution.

Further, we emphasize that a single Trotter step requires fewer than $8 \times 8 = 64$ CNOT gates due to the fixed boundary conditions. Each plaquette requires 2^n CNOT gates, where n is the number of adjacent plaquettes which are dynamical. For our setup, we therefore estimate the total number of CNOT gates as $2 \times 2 + 4 \times 4 + 2 \times 8 = 36$ for a single Trotter step and 360 for the full time evolution depicted here up to $tJ = 10$, or 144 for $tJ = 4$. Estimating the current two-qubit gate fidelities to be about 0.99%, we would achieve about $0.99^{144} = 0.24$ for

four Trotter steps. In principle, the requirement of more SWAP gates could make the actual simulation challenging.

We should note, however, that the estimate offered above is very qualitative. It has already been noted that a proper assessment of the resource requirements on noisy intermediate-scale quantum devices often does not give the entire picture, since appropriate error-correction methodologies can be adopted to significantly improve the raw results from experiments [72–74].

IV. FUTURE DIRECTIONS

The results about the phases and the phase diagram of the model presented here immediately open up several avenues of future research. We have noted the existence of different symmetry breakings on either side of the phase transition. It would be very instructive to study how the flux tubes joining the static charge-anticharge pair rearrange themselves as the phase transition is crossed in real time. Figure 2 suggests that the interior of the strands consists of the bulk phase that is realized on the other side of the transition such that the string interior and the surrounding bulk must exchange their roles during this transition.

The rich string dynamics of the simple U(1) quantum link model provides additional motivation to push the experimental frontier forward in this direction, towards the ultimate goal of quantum simulating QCD itself [75], and understand its dynamical properties, such as thermalization, which are beyond the reach of classical simulations. It might also be interesting to adapt the model to the two-dimensional Rydberg atom setups available [76] for quantum simulation. The experimental results will help us to better understand the real-time dynamics of confining strings, in particular with regard to their thermalization.

ACKNOWLEDGMENTS

[1] M. Lüscher, K. Symanzik, and P. Weisz, Anomalies of the free loop wave equation in the WKB approximation, Nucl. Phys. B **173**, 365 (1980).

[2] M. Lüscher, Symmetry breaking aspects of the roughening transition in gauge theories, Nucl. Phys. B **180**, 317 (1981).

[3] M. Lüscher, G. Münster, and P. Weisz, How thick are chromoelectric flux tubes? Nucl. Phys. B **180**, 1 (1981).

[4] M. Lüscher and P. Weisz, Locality and exponential error reduction in numerical lattice gauge theory, J. High Energy Phys. 09 (2001) 010.

[5] M. Lüscher and P. Weisz, Quark confinement and the bosonic string, J. High Energy Phys. 07 (2002) 049.

[6] K. J. Juge, J. Kuti, and C. Morningstar, Fine Structure of the QCD String Spectrum, Phys. Rev. Lett. **90**, 161601 (2003).

[7] P. Majumdar, The String spectrum from large Wilson loops, Nucl. Phys. B **664**, 213 (2003).

[8] M. Lüscher and P. Weisz, String excitation energies in SU(N) gauge theories beyond the free-string approximation, J. High Energy Phys. 07 (2004) 014.

[9] B. B. Brandt and P. Majumdar, Spectrum of the QCD flux tube in 3d SU(2) lattice gauge theory, Phys. Lett. B **682**, 253 (2009).

[10] F. Gliozzi, M. Pepe, and U.-J. Wiese, The Width of the Confining String in Yang-Mills Theory, Phys. Rev. Lett. **104**, 232001 (2010).

[11] B. B. Brandt and M. Meineri, Effective string description of confining flux tubes, Int. J. Mod. Phys. A **31**, 1643001 (2016).

[12] D. Horn, Finite matrix models with continuous local gauge invariance, Phys. Lett. B **100**, 149 (1981).

[13] P. Orland and D. Rohrlich, Lattice gauge magnets: Local isospin from spin, Nucl. Phys. B **338**, 647 (1990).

[14] S. Chandrasekharan and U.-J. Wiese, Quantum link models: A Discrete approach to gauge theories, Nucl. Phys. B **492**, 455 (1997).

[15] R. Brower, S. Chandrasekharan, and U.-J. Wiese, QCD as a quantum link model, Phys. Rev. D **60**, 094502 (1999).

[16] R. Brower, S. Chandrasekharan, S. Riederer, and U.-J. Wiese, D-theory: Field quantization by dimensional reduction of discrete variables, Nucl. Phys. B **693**, 149 (2004).

[17] K. G. Wilson, Confinement of quarks, Phys. Rev. D **10**, 2445 (1974).

[18] D. Banerjee, F.-J. Jiang, P. Widmer, and U.-J. Wiese, in *Proceedings of the 31st International Symposium on Lattice Field Theory, Mainz, 2013* (SISSA, Trieste, 2014), Vol. 187, p. 333.

[19] D. Banerjee, F.-J. Jiang, P. Widmer, and U.-J. Wiese, The $(2 + 1)$-d $U(1)$ quantum link model masquerading as deconfined criticality, J. Stat. Mech. (2013) P12010.

[20] D. Banerjee, F.-J. Jiang, T. Z. Olesen, P. Orland, and U.-J. Wiese, From the $SU(2)$ quantum link model on the honeycomb lattice to the quantum dimer model on the kagome lattice: Phase transition and fractionalized flux strings, Phys. Rev. B **97**, 205108 (2018).

[21] N. Shannon, G. Misguich, and K. Penc, Cyclic exchange, isolated states, and spinon deconfinement in an XXZ Heisenberg model on the checkerboard lattice, Phys. Rev. B **69**, 220403(R) (2004).

[22] L. Cardarelli, S. Greschner, and L. Santos, Hidden Order and Symmetry Protected Topological States in Quantum Link Ladders, Phys. Rev. Lett. **119**, 180402 (2017).

[23] Y.-P. Huang, D. Banerjee, and M. Heyl, Dynamical Quantum Phase Transitions in U(1) Quantum Link Models, Phys. Rev. Lett. **122**, 250401 (2019).

[24] F. Tschirsich, S. Montangero, and M. Dalmonte, Phase diagram and conformal string excitations of square ice using gauge invariant matrix product states, SciPost Phys. **6**, 028 (2019).

[25] R. C. Brower, D. Berenstein, and H. Kawai, Lattice gauge theory for a quantum computer, PoS **(LATTICE2019)**, 112 (2019).

[26] T. Felser, P. Silvi, M. Collura, and S. Montangero, Two-Dimensional Quantum-Link Lattice Quantum Electrodynamics at Finite Density, Phys. Rev. X **10**, 041040 (2020).

[27] L. Cardarelli, S. Greschner, and L. Santos, Deconfining Disordered Phase in Two-Dimensional Quantum Link Models, Phys. Rev. Lett. **124**, 123601 (2020).

[28] A. Celi, B. Vermersch, O. Viyuela, H. Pichler, M. D. Lukin, and P. Zoller, Emerging Two-Dimensional Gauge Theories in Rydberg Configurable Arrays, Phys. Rev. X **10**, 021057 (2020).

[29] D. Luo, J. Shen, M. Highman, B. K. Clark, B. DeMarco, A. X. El-Khadra, and B. Gadway, Framework for simulating gauge theories with dipolar spin systems, Phys. Rev. A **102**, 032617 (2020).

[30] T. V. Zache, M. Van Damme, J. C. Halimeh, P. Hauke, and D. Banerjee, Achieving the continuum limit of quantum link lattice gauge theories on quantum devices, arXiv:2104.00025.

[31] F. M. Surace, P. P. Mazza, G. Giudici, A. Lerose, A. Gambassi, and M. Dalmonte, Lattice Gauge Theories and String Dynamics in Rydberg Atom Quantum Simulators, Phys. Rev. X **10**, 021041 (2020).

[32] Y.-T. Kang, C.-Y. Lo, S. Yin, and P. Chen, Kibble-Zurek mechanism in a quantum link model, Phys. Rev. A **101**, 023610 (2020).

[33] J. C. Halimeh, R. Ott, I. P. McCulloch, B. Yang, and P. Hauke, Robustness of gauge-invariant dynamics against defects in ultracold-atom gauge theories, Phys. Rev. Research **2**, 033361 (2020).

[34] D. Banerjee and A. Sen, Quantum Scars from Zero Modes in an Abelian Lattice Gauge Theory, Phys. Rev. Lett. **126**, 220601 (2021).

[35] M. Van Damme, H. Lang, P. Hauke, and J. C. Halimeh, Reliability of lattice gauge theories in the thermodynamic limit, arXiv:2104.07040.

[36] D. S. Rokhsar and S. A. Kivelson, Superconductivity and the Quantum Hard-Core Dimer Gas, Phys. Rev. Lett. **61**, 2376 (1988).

[37] D. Banerjee, M. Bögli, C. P. Hofmann, F.-J. Jiang, and U.-J. Wiese, Interfaces, strings, and a soft mode in the square lattice quantum dimer model, Phys. Rev. B **90**, 245143 (2014).

[38] D. Banerjee, M. Bögli, C. P. Hofmann, F.-J. Jiang, and U.-J. Wiese, Finite-volume energy spectrum, fractionalized strings, and low-energy effective field theory for the quantum dimer model on the square lattice, Phys. Rev. B **94**, 115120 (2016).

[39] U.-J. Wiese, Ultracold quantum gases and lattice systems: Quantum simulation of lattice gauge theories, Ann. Phys. **525**, 777 (2013).

[40] M. C. Bañuls *et al.*, Simulating lattice gauge theories within quantum technologies, Eur. Phys. J. D **74**, 165 (2020).

[41] U.-J. Wiese, From quantum link models to D-theory: A resource efficient framework for the quantum simulation and computation of gauge theories, Philos. Trans. R. Soc. A **380**, 20210068 (2021).

[42] D. Banerjee, M. Bögli, M. Dalmonte, E. Rico, P. Stebler, U.-J. Wiese, and P. Zoller, Atomic Quantum Simulation of U(N) and SU(N) Non-Abelian Lattice Gauge Theories, Phys. Rev. Lett. **110**, 125303 (2013).

[43] D. Banerjee, M. Dalmonte, M. Müller, E. Rico, P. Stebler, U.-J. Wiese, and P. Zoller, Atomic Quantum Simulation of Dynamical Gauge Fields Coupled to Fermionic Matter: From String Breaking to Evolution after a Quench, Phys. Rev. Lett. **109**, 175302 (2012).

[44] A. W. Glätzle, M. Dalmonte, R. Nath, I. Rousochatzakis, R. Moessner, and P. Zoller, Quantum Spin-Ice and Dimer Models with Rydberg Atoms, Phys. Rev. X **4**, 041037 (2014).

[45] D. Marcos, P. Widmer, E. Rico, M. Hafezi, P. Rabl, U.-J. Wiese, and P. Zoller, Two-dimensional lattice gauge theories with superconducting quantum circuits, Ann. Phys. (NY) **351**, 634 (2014).

[46] E. A. Martinez, C. A. Muschik, P. Schindler, D. Nigg, A. Erhard, M. Heyl, P. Hauke, M. Dalmonte, T. Monz, and P. Zoller, Real-time dynamics of lattice gauge theories with a few-qubit quantum computer, Nature (London) **534**, 516 (2016).

[47] H. Bernien, S. Schwartz, A. Keesling, H. Levine, A. Omran, H. Pichler, S. Choi, A. S. Zibrov, M. Endres, M. Greiner, V. Vuleti, and M. D. Lukin, Probing many-body dynamics on a 51-atom quantum simulator, Nature (London) **551**, 579 (2017).

[48] N. Klco, E. F. Dumitrescu, A. J. McCaskey, T. D. Morris, R. C. Pooser, M. Sanz, E. Solano, P. Lougovski, and M. J. Savage, Quantum-classical computation of Schwinger model dynamics using quantum computers, Phys. Rev. A **98**, 032331 (2018).

[49] H.-H. Lu, N. Klco, J. M. Lukens, T. D. Morris, A. Bansal, A. Ekström, G. Hagen, T. Papenbrock, A. M. Weiner, and M. J. Savage, Simulations of subatomic many-body physics on a quantum frequency processor, Phys. Rev. A **100**, 012320 (2019).

[50] C. Schweizer, F. Grusdt, M. Berngruber, L. Barbiero, E. Demler, N. Goldman, I. Bloch, and M. Aidelsburger, Floquet approach to Z_2 lattice gauge theories with ultracold atoms in optical lattices, Nat. Phys. **15**, 1168 (2019).

[51] F. Görg, K. Sandholzer, J. Minguzzi, R. Desbuquois, M. Messer, and T. Esslinger, Realization of density-dependent Peierls phases to engineer quantized gauge fields coupled to ultracold matter, Nat. Phys. **15**, 1161 (2019).

[52] A. Mil, T. V. Zache, A. Hegde, A. Xia, R. P. Bhatt, M. K. Oberthaler, P. Hauke, J. Berges, and F. Jendrzejewski, A scalable realization of local U(1) gauge invariance in cold atomic mixtures, Science **367**, 1128 (2020).

[53] B. Yang, H. Sun, R. Ott, H.-Y. Wang, T. V. Zache, J. C. Halimeh, Z.-S. Yuan, P. Hauke, and J.-W. Pan, Observation of gauge invariance in a 71-site Bose-Hubbard quantum simulator, Nature (London) **587**, 392 (2020).

[54] Y. Atas, J. Zhang, R. Lewis, A. Jahanpour, J. F. Haase, and C. A. Muschik, SU(2) hadrons on a quantum computer via a variational approach, Nat. Commun. **12**, 6499 (2021).

[55] P. Jurcevic *et al.*, Demonstration of quantum volume 64 on a superconducting quantum computing system, Quantum Sci. Technol. **6**, 025020 (2021).

[56] J. Chow, O. Dial, and J. Gambetta, *IBM Quantum breaks the 100-qubit processor barrier*, https://research.ibm.com/blog/127-qubit-quantum-processor-eagle (IBM Research, Armonk, 2021).

[57] P. Nation, H. Paik, A. Cross, and Z. Nazario, *The IBM Quantum heavy hex lattice*, https://research.ibm.com/blog/heavy-hex-lattice (IBM Research, Armonk, 2021).

[58] P. G. de Gennes, *The Physics of Liquid Crystals* (Clarendon Press, Oxford, 1974).

[59] P. E. Lammert, D. S. Rokhsar, and J. Toner, Topology and Nematic Ordering, Phys. Rev. Lett. **70**, 1650 (1993).

[60] P. E. Lammert, D. S. Rokhsar, and J. Toner, Topology and nematic ordering. I. A gauge theory, Phys. Rev. E **52**, 1778 (1995).

[61] K. Liu, J. Nissinen, Z. Nussinov, R.-J. Slager, K. Wu, and J. Zaanen, Classification of nematic order in 2+1 dimensions: Dislocation melting and $O(2)/Z_N$ lattice gauge theory, Phys. Rev. B **91**, 075103 (2015).

[62] K. Liu, J. Nissinen, R.-J. Slager, K. Wu, and J. Zaanen, Generalized Liquid Crystals: Giant Fluctuations and the Vestigial Chiral Order of I, O, and T Matter, Phys. Rev. X **6**, 041025 (2016).

[63] A. J. Beekman, J. Nissinen, K. Wu, K. Liu, R.-J. Slager, Z. Nussinov, V. Cvetkovic, and J. Zaanen, Dual gauge field theory of quantum liquid crystals in two dimensions, Phys. Rep. **683**, 1 (2017).

[64] G. 't Hooft, A property of electric and magnetic flux in non-Abelian gauge theories, Nucl. Phys. B **153**, 141 (1979).

[65] D. Banerjee, Recent progress on cluster and meron algorithms for strongly correlated systems, Indian J. Phys. **95**, 1669 (2021).

[66] B. B. Beard and U.-J. Wiese, Simulations of Discrete Quantum Systems in Continuous Euclidean Time, Phys. Rev. Lett. **77**, 5130 (1996).

[67] T. Senthil, A. Vishwanath, L. Balents, S. Sachdev, and M. P. A. Fisher, Deconfined quantum critical points, Science **303**, 1490 (2004).

[68] T. Senthil, L. Balents, S. Sachdev, A. Vishwanath, and M. P. A. Fisher, Quantum criticality beyond the Landau-Ginzburg-Wilson paradigm, Phys. Rev. B **70**, 144407 (2004).

[69] B. Zhao, P. Weinberg, and A. W. Sandvik, Symmetry enhanced first-order phase transition in a two-dimensional quantum magnet, Nat. Phys. **15**, 678 (2019).

[70] V. Gorbenko, S. Rychkov, and B. Zan, Walking, weak first-order transitions, and complex CFTs, J. High Energy Phys. 10 (2018) 108.

[71] C. J. Turner, A. A. Michailidis, D. A. Abanin, M. Serbyn, and Z. Papić, Quantum scarred eigenstates in a Rydberg atom chain: Entanglement, breakdown of thermalization, and stability to perturbations, Nat. Phys. **14**, 745 (2018).

[72] E. Huffman, M. G. Vera, and D. Banerjee, Real-time dynamics of plaquette models using NISQ hardware, arXiv:2109.15065.

[73] A. Rajput, A. Roggero, and N. Wiebe, Quantum error correction with gauge symmetries, arXiv:2112.05186.

[74] J. Mildenberger, W. Mruczkiewicz, J. C. Halimeh, Z. Jiang, and P. Hauke, Probing confinement in a Z_2 lattice gauge theory on a quantum computer, arXiv:2203.08905.

[75] U.-J. Wiese, Towards quantum simulating QCD, Nucl. Phys. A **931**, 246 (2014).

[76] S. Ebadi *et al.*, Quantum phases of matter on a 256-atom programmable quantum simulator, Nature (London) **595**, 227 (2021).